# Visualizing electrostatic gating effects in two-dimensional heterostructures

Paul V Nguyen,[1] Natalie C Teutsch*,[2] Nathan Wilson,[1] Joshua Kahn,[1] Xue Xia*,[2] Abigail J Graham*,[2] Viktor Kandyba,[3] Alessio Giampietri,[3] Alexei Barinov,[3] Gabriel C Constantinescu,[4] Nelson Yeung,[2] Nicholas D M Hine,[2] Xiaodong Xu,[1,5*] David H Cobden,[1*] Neil R Wilson*[2*]

[1]Department of Physics, University of Washington, Seattle, Washington 98195, USA

[2]Department of Physics, University of Warwick, Coventry, CV4 7AL, UK

[3]Elettra - Sincrotrone Trieste, S.C.p.A., Basovizza (TS), 34149, Italy

[4]TCM Group, Cavendish Laboratory, University of Cambridge, 19 JJ Thomson Avenue, Cambridge CB3 0HE, UK

[5]Department of Material Science and Engineering, University of Washington, Seattle, Washington 98195, USA

Submitted and accepted to Nature

**The ability to directly monitor the states of electrons in modern field-effect devices, for example imaging local changes in the electrical potential, Fermi level and band structure as a gate voltage is applied, could transform understanding of the device physics and function. Here we show that submicrometre angle-resolved photoemission spectroscopy[1–3] (μ-ARPES) applied to two-dimensional van der Waals heterostructures[4] affords this ability. In two-terminal graphene devices we observe a shift of the Fermi level across the Dirac point, with no detectable change in the dispersion, as a gate voltage is applied. In two-dimensional semiconductor devices we see the conduction band edge appear as electrons accumulate, thereby firmly establishing its energy and momentum. In the case of monolayer $WSe_2$ we observe that the band gap is renormalized downwards by several hundred meV, approaching the exciton energy, as the electrostatic doping increases. Both optical spectroscopy and μ-ARPES can be carried out on a single device, allowing definitive studies of the relationship between gate-controlled electronic and optical properties. The technique provides a powerful new means to study not only fundamental semiconductor physics but also intriguing phenomena such as topological transitions[5] and many-body spectral reconstructions under electrical control.**

In ARPES one measures the distribution of energy and momentum of electrons photoemitted from a solid sample subjected to a narrow-spectrum ultraviolet or X-ray excitation. This provides information about the energy and momentum of the initial occupied electron states, and hence the band structure and Fermi level. As electrons are emitted only from very near the sample surface, ARPES is not useful for studying conventional semiconductor devices. On the other hand, it is well suited to probing two-dimensional (2D) materials, and has been applied to films of graphene[6], transition metal dichalcogenides ($MX_2$, where M=Mo,W,Ta etc and X=S,Se,Te)[7,8], and others[9,10]. While the excitation spot size is typically measured in millimetres, efforts have been made in the last decade[2] to perform ARPES with a focused beam suitable for small or nonuniform samples. Micrometre-scale spot sizes (hence μ-ARPES) have been achieved in at least four commissioned synchrotron beamlines using Schwarzschild objectives[1], Fresnel zone plates[2,3], or capillary mirror optics[11]. μ-ARPES has allowed the study of atomically thin exfoliated flakes of 2D materials, which are typically tens of microns or less in size[12], and of heterostructures[4] made by stacking such flakes of different materials[13,14], revealing for example band offsets and interlayer hybridization[15–17]. Such 2D heterostructures can be made into electrical and optical devices[18] by incorporating metal electrodes, opening up the possibility of using μ-ARPES to monitor electronic structure in operating devices.

A major limitation of ARPES is that it probes only occupied electron states. A semiconductor sample must therefore be electron-doped in order to obtain a signal from the conduction band. Doping is usually achieved by depositing electropositive atoms such as alkali metals[6–8,13] on the surface. This

process cannot be controlled accurately and can only be reversed by high temperature annealing; moreover, it chemically perturbs the electronic structure and introduces disorder through the random distribution of dopants. In this work we demonstrate purely electrostatic doping, which has none of these disadvantages. We thereby obtain momentum-resolved electronic spectra and direct visualization of Fermi level shifts and band structure changes induced by applying a gate voltage.

We first demonstrate and validate the technique using graphene, then go on to apply it to the 2D $MX_2$ semiconductors which are of interest for valleytronics and other applications[18,19]. Although it is widely believed that all monolayer $MX_2$ semiconductors have a direct band gap at the corner of the hexagonal Brillouin zone, **K**, the location of the conduction band edge (CBE) is not known with certainty. This is illustrated by the wide range of reported band gap values for monolayer $WSe_2$, from 1.4 to 2.2 eV[8,20–24]. Also unclear is when the local conduction band minimum at the lower-symmetry point **Q** comes into play[21,25]. Using electrostatic doping in μ-ARPES, we confirm that the CBE is at **K** in all the monolayer semiconductors, $MoS_2$, $MoSe_2$, $WS_2$ and $WSe_2$, and in each case we obtain a measure of the band gap. We also study the layer-number dependence in $WSe_2$, finding that the CBE moves to **Q** in the bilayer, and measure for the first time the renormalization of the band structure on gating.

## 1. Electrostatic doping of graphene

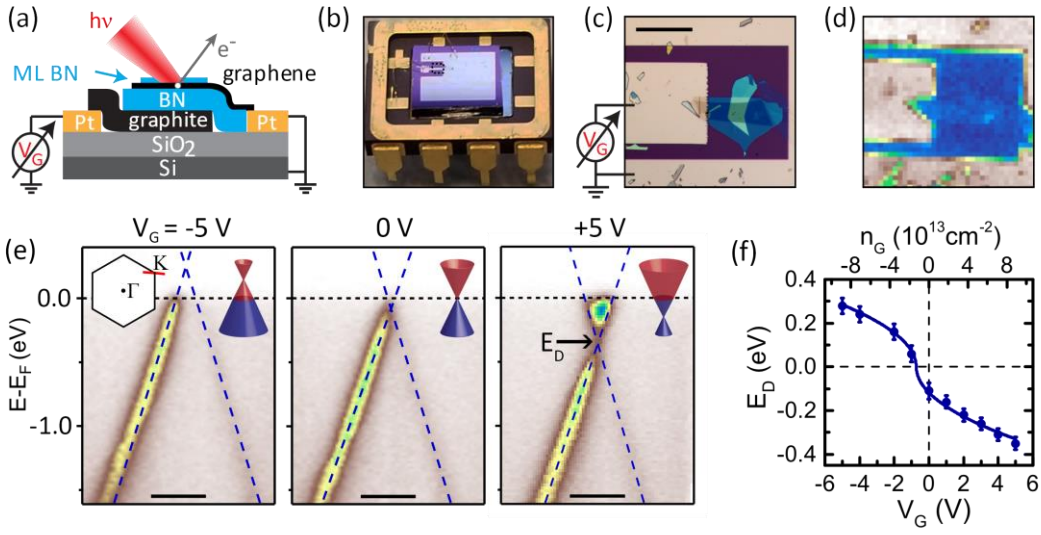


**Figure 1. Visualizing electrostatic gating of monolayer graphene.** (**a**) Schematic of a 2D heterostructure device with a stack comprising graphene encapsulated by BN on a graphite back gate. Photoemission is measured with a focused micron-size X-ray beam spot (see Methods). The graphene is grounded while a gate voltage $V_G$ is applied to the gate. (**b**) Optical image of a device mounted in a standard dual in-line package. (**c**) Optical zoom on the dotted box in (b) showing the stack, and (**d**) scanning photoemission microscopy (SPEM) image of the same area (scale bar, 50 μm). (**e**) Energy-momentum slices near the graphene K-point, along the red line in the inset Brillouin zone, at the labelled gate voltages. The dashed lines are linear dispersion fits; the Dirac point energy $E_D$ is deduced from their crossing point (scale bars, 0.2 Å$^{-1}$). (**f**) Gate dependence of $E_D$, with error bars obtained from the fitting procedure. The solid line is a fit based on the dispersion of graphene, with the gate-induced electron density $n_G$ shown on the top axis calculated from the capacitance (see Methods).

We first demonstrate gate-doping of monolayer graphene. A graphene sheet is capped by monolayer hexagonal boron nitride (BN), supported on a BN flake over a graphite gate (Fig. 1a), and located in a gap between two platinum electrodes on an $SiO_2$/Si substrate chip (Figs. 1b and 1c; see Methods). A similar structure with two contacts to the graphene would function as a high-mobility transistor[26]. Scanning photoemission microscopy (SPEM) is used to locate the sample in the ARPES chamber (Fig. 1d; see Methods). Fig. 1e shows energy, $E - E_F$, vs momentum for a slice through the Dirac cone near the graphene zone corner **K**, acquired at a series of gate voltages $V_G$ at 105 K. As expected, the Dirac point energy $E_D$ shifts from above the Fermi level $E_F$ at $V_G$ = -5 V to below $E_F$ at

+5 V. Fitting a linear dispersion, $E(\boldsymbol{k}) = E_D \pm \hbar v_F k$ (dashed lines), gives $E_D$ and the Fermi velocity $v_F$. We find $v_F = (9.3 \pm 0.1) \times 10^5$ ms$^{-1}$ at $V_G = 0\ V$, with a weak $V_G$ dependence (see Extended Data). The variation of $E_D$ with $V_G$ (Fig. 1f) is consistent with the expected form for this dispersion (solid line, see Methods). No modification of the dispersion near $E_D$, which could arise due to interactions, is detectable with the current spectral resolution.

The consistency of the above properties with the graphene literature, together with the observation that the spectrum is undistorted as $V_G$ is changed, implies that the photoelectron trajectories are not affected by stray electric fields due to the gate voltage or charging effects. We conclude that the technique produces accurate local electronic spectra during live electrostatic gating.

**2. Electrostatic population of the conduction band in 2D semiconductors**

An $MX_2$ flake can be incorporated in the stack on top of the BN, partially overlapping graphene that acts as a contact to it (Fig. 2a). Figures 2b and c are optical and SPEM images of a device with a $WSe_2$ flake that has monolayer (1L), bilayer (2L) and trilayer (3L) regions. Figures 2d-f are momentum slices obtained with the beam spot on each of the regions, respectively, along $\mathbf{\Gamma} - \mathbf{K}$ of the $WSe_2$ Brillouin zone at 100 K (Fig. 2g, inset). As expected, at $V_G = 0$ (upper row) only the valence bands can be seen. Their evolution with layer number is consistent with the literature[27] and matches the overlaid density functional theory (DFT) predictions well (Methods). At $V_G = +3.35$ V (lower row) an additional spot appears near $E_F$. The size of this conduction band feature is determined solely by the instrument resolution. In 1L $WSe_2$ the spot is located at $\mathbf{K}$, whereas in 2L and 3L it is at $\mathbf{Q}$ (see Fig. 2g). This is consistent with evidence from photoluminescence[25] that the gap is direct at $\mathbf{K}$ in the monolayer but indirect for 2+ layers.

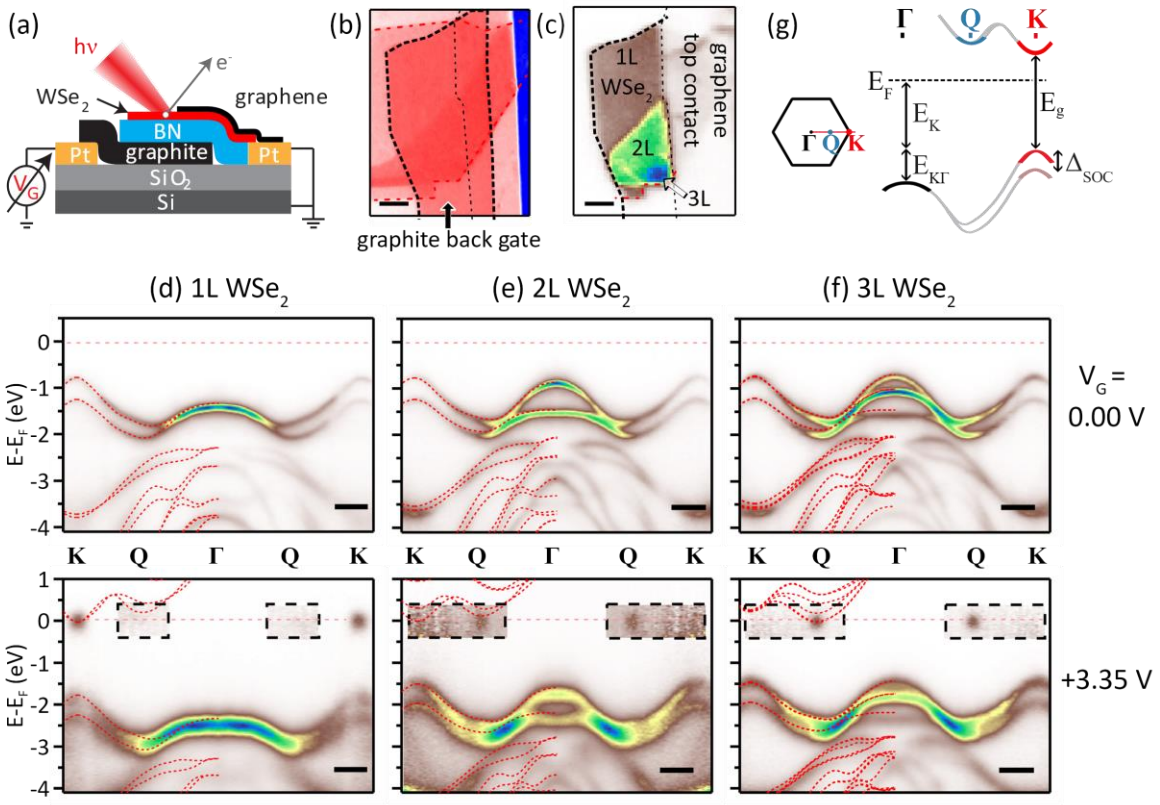


**Figure 2. Layer-number dependent conduction band edge (CBE) in $WSe_2$.** (**a**) Schematic of a device incorporating a $WSe_2$ flake, with overlapping graphene top contact grounded and gate voltage $V_G$ applied to the graphite back gate. (**b**) Optical and (**c**) SPEM images of $WSe_2$ Device 1 ($d_{BN} = 7.4 \pm 0.5$ nm), with monolayer, bilayer and trilayer regions identified (scale bars, 5 μm). (**d**)-(**f**) Energy-momentum slices along $\mathbf{\Gamma} - \mathbf{K}$ for 1L, 2L, and 3L regions respectively. The upper panels are at $V_G = 0$ and the lower ones at $V_G = +3.35\ V$. The intensity in the dashed boxes is multiplied by 20. The fuzzy spots signal population of the CBE. Scale bars, 0.3 Å$^{-1}$. The data have been reflected about $\mathbf{\Gamma}$ to aid

comparison with DFT predictions (red dashed lines). (**g**) Brillouin zone of $MX_2$, and schematic of bands along $\mathbf{\Gamma} - \mathbf{K}$ showing definitions of the energy parameters discussed in the text.

Table 1 displays the band parameters for 1L–3L $WSe_2$ as well as for other monolayer $MX_2$ species, derived[15] from measurements on this and other devices (see SI section S5). The band gap, $E_g = E_C - E_K$, where $E_C$ is the energy of the CBE, was determined at a doping level of $n_G \approx 10^{13}$ cm$^{-2}$ for which $E_F - E_C \sim 30$ meV (see Methods). We also list the simultaneously determined hole effective mass $m_K^*$, valence band edge $E_K$, spin-orbit splitting $\Delta_{SOC}$, and $E_{K\Gamma}$ as defined in Fig. 2g, all measured for the first time on an hBN substrate with no cap and with greater precision than in previous reports.

| | $\Delta_{SOC}$ (eV) | $E_K$ ($V_G = 0$) (eV) | $E_{K\Gamma}$ ($V_G = 0$) (eV) | $m_K^*/m_e$ | $E_g$ (eV) |
|---|---|---|---|---|---|
| 1L $MoS_2$ | $0.17 \pm 0.04$ | $1.93 \pm 0.02$ | $0.14 \pm 0.04$ | $0.7 \pm 0.1$ | $2.07 \pm 0.05$ |
| 1L $MoSe_2$ | $0.22 \pm 0.03$ | $1.04 \pm 0.02$ | $0.48 \pm 0.03$ | $0.5 \pm 0.1$ | $1.64 \pm 0.05$ |
| 1L $WS_2$ | $0.45 \pm 0.03$ | $1.43 \pm 0.02$ | $0.39 \pm 0.02$ | $0.5 \pm 0.1$ | $2.03 \pm 0.05$ |
| 1L $WSe_2$ | $0.485 \pm 0.010$ | $0.80 \pm 0.01$ | $0.62 \pm 0.01$ | $0.42 \pm 0.05$ | $1.79 \pm 0.03$ |
| 2L $WSe_2$ | $0.501 \pm 0.010$ | $0.75 \pm 0.01$ | $0.14 \pm 0.01$ | $0.41 \pm 0.05$ | $1.51 \pm 0.03$ * |
| 3L $WSe_2$ | $0.504 \pm 0.010$ | $0.74 \pm 0.01$ | $0.00 \pm 0.01$ | $0.40 \pm 0.05$ | $1.46 \pm 0.03$ * |

*indirect, with CBE at $\boldsymbol{Q}$

**Table 1. Measured band structure parameters of $MX_2$ semiconductors.** As defined in Fig. 2g, $\Delta_{SOC}$ is the spin-orbit splitting of the valence band at **K**; $E_K$ is the valence band edge at $V_G = 0$; $E_{K\Gamma} = E_K - E_\Gamma$ is the difference between the valence band edges at **K** and **Γ** at $V_G = 0$; $m_K^*$ is the effective mass of the valence band edge at **K** in units of the free electron mass $m_e$; and $E_g$ is the band gap measured at gate-induced electron density $n_G = 1.0 \pm 0.2 \times 10^{12}$ cm$^{-2}$. The stage temperature was 100 K for the $WSe_2$ and 105 K for the others.

## 3. Gate dependence of the electronic structure of a semiconducting monolayer

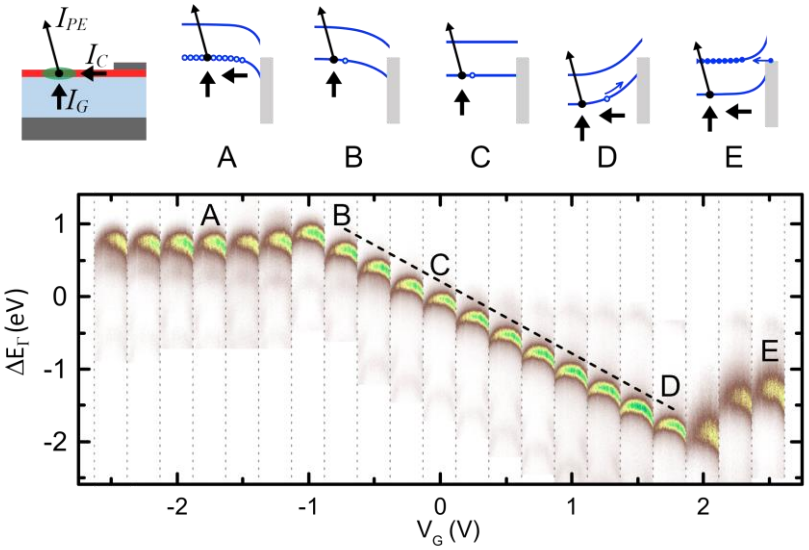


**Figure 3. Electrostatic gating of monolayer $WSe_2$.** Each vertical strip is an energy-momentum slice, 0.6 Å$^{-1}$ wide, through **Γ** in $WSe_2$ Device 2 ($d_{hBN} = 6.0 \pm 0.5$ nm) measured at the gate voltage shown on the bottom axis. $\Delta E_\Gamma$ is the photoelectron kinetic energy measured relative to the Γ-point maximum at $V_G = 0$. The dashed line has slope $-1/e$. Above left is a device schematic indicating the photoemission current $I_{PE}$ from the beam spot, current $I_C$ from the graphene contact, and current $I_G$ from the gate through the BN due to photoconductivity. The schematic band diagrams indicate the situations at the gate voltages labelled A-E. The gray rectangle is the graphene Fermi sea, the blue lines are the $WSe_2$ conduction and valence band edges, and the smaller arrows indicate when $I_G$ and $I_C$ are significant.

We now investigate the full gate dependence of μ-ARPES spectra. Figure 3 shows the behavior of the top of the valence band at **Γ**, where the photoemission signal is strongest, for monolayer $WSe_2$

Device 2. At low $V_G$ (range labelled B-C-D) the spectrum shifts nearly linearly with a slope $-1/e$, where $e$ is the electron charge, implying that the electrostatic potential in the $WSe_2$ tracks the gate potential when it is undoped. For $V_G$ > +2.1 V (E) or < -1.5 V (A) it becomes almost independent of $V_G$, implying that these are the thresholds for electron and hole accumulation, respectively. The behavior can be understood in more detail with reference to the corresponding band diagrams shown above, taking into account the balance of the current of photoemitted electrons, $I_{PE}$, the currents into the beam spot from the contact, $I_C$, and the gate, $I_G$, as indicated in the sketch at the top left (see Methods).

Note that no change in spectral widths is seen as long as the $WSe_2$ is insulating (range B-D in Fig. 3), but above threshold (range D-E) all features are smeared in energy by a similar amount. This can be explained by inhomogeneous broadening due to variation of the potential across the beam spot associated with lateral current flow in the $WSe_2$. Refinement of the technique to reduce this effect may allow studies of changes in intrinsic broadening with doping.

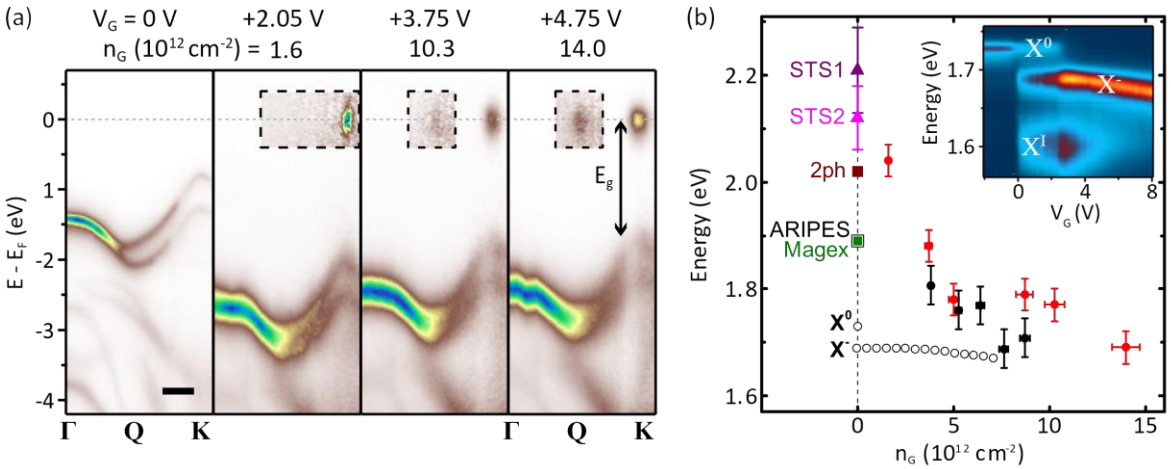


**Figure 4. Renormalization of the band gap and comparison with optical spectroscopy. (a)** Energy-momentum slices along **Γ-K** for monolayer $WSe_2$ in Device 1 at a series of $V_G$, with doping $n_G$ also shown (scale bar, 0.3 Å$^{-1}$). The intensity in the dashed box is multiplied by 20 at +2.05 V and by 40 at higher $V_G$. The definition of the band gap, $E_g$, is indicated. **(b)** Band gap dependence on $n_G$ for Device 1 (red) and also Device 3 ($d_{BN} = 24.5 \pm 0.5$ nm, solid black circles) at 100 K. Also plotted (black open circles) are the photoluminescence peak positions for the neutral exciton ($X^0$) and negative trion ($X^-$) in Device 3 at the same temperature. The inset shows the photoluminescence data, with an impurity-bound exciton peak $X^I$ also labelled. The points plotted at $n_G = 0$ are measurements of the band gap from other techniques taken from the literature: STS1[20] (purple triangle) and STS2[21] (pink triangle) are from scanning tunnelling spectroscopy measurements, on graphite at T= 4.5 K and 77 K respectively; 2ph (brown square) is from two-photon absorption[22], on $SiO_2$ at 300 K; ARIPES (black open square) is from inverse photoemission[23], on sapphire at 300 K; and Magex (green solid square) is from magneto-optical measurements[24], encapsulated in BN at 4 K.

Figure 4a shows spectra from monolayer $WSe_2$ Device 1 at $V_G = 0$ (for reference) and at selected gate voltages well above threshold (about +1.5 V). In this regime we derive the gate doping $n_G$, also shown, from the gate capacitance and threshold voltage (see Methods). The CBE becomes visible at **K** for $n_G > \sim 10^{12}$ cm$^{-2}$ and at **Q** for $n_G > \sim 10^{13}$ cm$^{-2}$, when $E_K$ is roughly 30 meV below $E_F$. We conclude that the conduction band minimum at **Q** is higher than that at **K**. Scanning tunnelling spectroscopy[21] also indicates that for 1L $WSe_2$ these minima are very close. The form of the valence bands does not change discernibly with increasing $n_G$, but they shift upwards in energy while the CBE is pinned at $E_F$, implying that the band gap decreases.

Optical spectroscopy can be performed on the same devices, and under the same conditions, as the μ–ARPES measurements, eliminating uncertainties due to differences in sample quality, dielectric environment, gate voltage and temperature[28–30]. Figure 4b shows both the μ-ARPES determination of $E_g$ (black solid circles) and the photoluminescence peak positions (black empty circles), $E_{X^0}$ and $E_{X^-}$,

for neutral ($X^0$) and charged ($X^-$) excitons, for monolayer $WSe_2$ Device 3 as a function of gate doping at 100 K. Also shown are the values of $E_g$ from Device 1 (red solid circles), which agree to within the uncertainty. It is apparent that $E_g$ decreases systematically, by ~400 meV, as $n_G$ rises to $1.5 \times 10^{13}$ $cm^{-2}$. Such renormalization of the band gap with static doping is expected to occur in a semiconductor as a result of free-carrier screening[31], though it is has not previously been so accessible to experiments.

Also plotted in Fig. 4b are values of the band gap at $n_G = 0$ inferred from several other techniques. An extrapolation of $E_g$ measured by μ-ARPES to $n_G = 0$ is consistent with scanning tunneling spectroscopy (STS) measurements which put it in the range 2.1-2.2 eV. Comparison with $E_{X^0}$ supports arguments that the binding energy of neutral excitons in this material is very large[28], at several hundred meV. $E_g$ decreases much faster than $E_{X^-}$ with doping, implying dramatic weakening of the exciton binding which is another expected effect of free-carrier screening[29]. Finally, the still smaller values of $E_g$ reported in monolayers doped with alkali metals (down to 1.4 eV for 1L $WSe_2$) are consistent with an extrapolation the renormalization process to higher $n_G$[7,8].

The ability to measure changes in the electronic bands in 2D field-effect devices opens up many interesting possibilities. For example, it could be used to study electric-field tuning of the bands across topological phase transitions[5]; to investigate the doping dependence of spectra in correlated electron systems such as in superconductors, Mott insulators, and charge-density-wave materials; to observe spectral reconstructions in structures with moiré superlattice modulations[32]; and, with the addition of circularly polarized light or a spin-resolved spectrometer, to study electrically controlled magnetic phenomena[33].

**References**


1. Dudin, P. *et al.* Angle-resolved photoemission spectroscopy and imaging with a submicrometre probe at the SPECTROMICROSCOPY-3.2L beamline of Elettra. *J. Synchrotron Radiat.* **17**, 445–450 (2010).
2. Rotenberg, E. & Bostwick, A. microARPES and nanoARPES at diffraction-limited light sources: opportunities and performance gains. *J. Synchrotron Radiat.* **21**, 1048–1056 (2014).
3. Iwasawa, H. *et al.* Buried double CuO chains in $YBa_2Cu_4O_8$ uncovered by nano-ARPES. *J. Phys. Condens. Matter* **4**, 9015–9022 (2019).
4. Novoselov, K. S., Mishchenko, A., Carvalho, A. & Castro Neto, A. H. 2D materials and van der Waals heterostructures. *Science.* **353**, aac9439 (2016).
5. Tong, Q. *et al.* Topological mosaics in moiré superlattices of van der Waals heterobilayers. *Nat. Phys.* **13**, 356–362 (2017).
6. Bostwick, A., Ohta, T., Seyller, T., Horn, K. & Rotenberg, E. Quasiparticle dynamics in graphene. *Nat. Phys.* **3**, 36–40 (2007).
7. Riley, J. M. *et al.* Negative electronic compressibility and tunable spin splitting in $WSe_2$. *Nat. Nanotechnol.* **10**, 1043–1047 (2015).
8. Zhang, Y. *et al.* Electronic Structure, Surface Doping, and Optical Response in Epitaxial $WSe_2$ Thin Films. *Nano Lett.* **16**, 2485–2491 (2016).
9. Kim, J. *et al.* Observation of tunable band gap and anisotropic Dirac semimetal state in black phosphorus. *Science.* **349**, 723–726 (2015).
10. Tang, S. *et al.* Quantum spin Hall state in monolayer 1T'-$WTe_2$. *Nat. Phys.* **13**, 683–687 (2017).
11. Koch, R. J. *et al.* Nano focusing of soft X-rays by a new capillary mirror optic. *Synchrotron Radiat. News* **31**, 50–52 (2018).
12. Zhang, H. *et al.* Resolving Deep Quantum-Well States in Atomically Thin 2H-$MoTe_2$ Flakes by Nanospot Angle-Resolved Photoemission Spectroscopy. *Nano Lett.* **18**, 4664–4668 (2018).
13. Katoch, J. *et al.* Giant spin-splitting and gap renormalization driven by trions in single-layer $WS_2$/h-BN heterostructures. *Nat. Phys.* **14**, 355–359 (2018).
14. Cucchi, I. *et al.* Microfocus Laser–Angle-Resolved Photoemission on Encapsulated Mono-, Bi-, and Few-Layer 1T'-$WTe_2$. *Nano Lett.* **19**, 554–560 (2019).
15. Wilson, N. R. *et al.* Determination of band offsets, hybridization, and exciton binding in 2D

semiconductor heterostructures. *Sci. Adv.* **3**, e1601832 (2017).
16. Jin, W. *et al.* Tuning the electronic structure of monolayer graphene/ $MoS_2$ van der Waals heterostructures via interlayer twist. *Phys. Rev. B* **92**, 201409 (2015).
17. Pierucci, D. *et al.* Band Alignment and Minigaps in Monolayer $MoS_2$ -Graphene van der Waals Heterostructures. *Nano Lett.* **16**, 4054–4061 (2016).
18. Liu, Y. *et al.* Van der Waals heterostructures and devices. *Nature Reviews Materials* **1**, 16042 (2016).
19. Schaibley, J. R. *et al.* Valleytronics in 2D materials. *Nat. Rev. Mater.* **1**, 16055 (2016).
20. Yankowitz, M., McKenzie, D. & LeRoy, B. J. Local Spectroscopic Characterization of Spin and Layer Polarization in $WSe_2$. *Phys. Rev. Lett.* **115**, 136803 (2015).
21. Zhang, C. *et al.* Probing Critical Point Energies of Transition Metal Dichalcogenides: Surprising Indirect Gap of Single Layer $WSe_2$. *Nano Lett.* **15**, 6494–6500 (2015).
22. He, K. *et al.* Tightly Bound Excitons in Monolayer $WSe_2$. *Phys. Rev. Lett.* **113**, 026803 (2014).
23. Park, S. *et al.* Direct determination of monolayer $MoS_2$ and $WSe_2$ exciton binding energies on insulating and metallic substrates. *2D Mater.* **5**, 025003 (2018).
24. Stier, A. V. *et al.* Magnetooptics of exciton Rydberg states in a monolayer semiconductor. *Phys. Rev. Lett.* **120**, 057405 (2018).
25. Zhao, W., Ribeiro, R. M. & Eda, G. Electronic Structure and Optical Signatures of Semiconducting Transition Metal Dichalcogenide Nanosheets. *Acc. Chem. Res.* **48**, 91–99 (2015).
26. Mayorov, A. S. *et al.* Micrometer-Scale Ballistic Transport in Encapsulated Graphene at Room Temperature. *Nano Lett.* **11**, 2396–2399 (2011).
27. Liu, G., Xiao, D., Yao, Y., Xu, X. & Yao, W. Electronic structures and theoretical modelling of two-dimensional group-VIB transition metal dichalcogenides. *Chem. Soc. Rev.* **44**, 2643–2663 (2015).
28. Ugeda, M. M. *et al.* Giant bandgap renormalization and excitonic effects in a monolayer transition metal dichalcogenide semiconductor. *Nat. Mater.* **13**, 1091–1095 (2014).
29. Gao, S., Liang, Y., Spataru, C. D. & Yang, L. Dynamical Excitonic Effects in Doped Two-Dimensional Semiconductors. *Nano Lett.* **16**, 5568–5573 (2016).
30. Raja, A. *et al.* Coulomb engineering of the bandgap and excitons in two-dimensional materials. *Nat. Commun.* **8**, 15251 (2017).
31. Gao, S. & Yang, L. Renormalization of the quasiparticle band gap in doped two-dimensional materials from many-body calculations. *Phys. Rev. B* **96**, 155410 (2017).
32. Cao, Y. *et al.* Magic-angle graphene superlattices: a new platform for unconventional superconductivity. *Nature* **556**, 43–50 (2018).
33. Wang, H., Fan, F., Zhu, S. & Wu, H. Doping enhanced ferromagnetism and induced half-metallicity in $CrI_3$ monolayer. *EPL* **114**, 47001 (2016).

**Acknowledgements.**

The Engineering and Physical Sciences Research Council is acknowledged for support through EP/P01139X/1 and a studentship for NCT (EP/M508184/1). XXia was supported by a University of Warwick studentship. DHC and PVN were supported by US Department of Energy, Office of Basic Energy Sciences, Division of Materials Sciences and Engineering, award DE-SC0002197 and the Pro-QM Energy Frontiers Research Center. PVN and JK were also supported in part by NSF MRSEC award 1719797. XXu and NPW are supported by Department of Energy, Basic Energy Sciences, Materials Sciences and Engineering Division (DE-SC0018171). NDMH and GCC acknowledge the support of the Winton Programme for the Physics of Sustainability. Computing resources were provided by the Darwin Supercomputer of the University of Cambridge High Performance Computing Service. GCC acknowledges the support of the Cambridge Trust European Scholarship.

**Author contributions.**

NRW, XXu and DHC conceived and supervised the project. PVN, JK and NW fabricated the samples. NCT, NRW, PVN, XXia, AJG, VK, AG and AB collected μ-ARPES data. NCT, NRW and PVN analyzed μ-ARPES data, with input from AB. NPW acquired photoluminescence data. NDMH, NY and GCC performed the band structure calculations. DHC, NRW, PVN and XXu wrote the paper with input from all authors.

**Competing interests.**

The authors declare no competing interests.

**Materials & Correspondence.**

Correspondence to cobden@uw.edu, xuxd@uw.edu, neil.wilson@warwick.ac.uk

**Methods**

**Sample fabrication.** Standard micro-mechanical exfoliation and dry transfer[34] with polycarbonate film-based stamping were used. The smaller electrode contacts the graphite gate, as indicated in the optical micrograph in Fig. 1c. The larger electrode, which contacts the graphene, is grounded and covers most of the chip to minimize electrostatic distortion of the photoelectron spectrum when applying a gate voltage. The sample substrates are mounted in dual-inline packages using ultra-high vacuum and high-temperature compatible silver epoxy and wire-bonded. Bare wire is wrapped around the package pins, fixed using the epoxy, and used to contact to leads on the ARPES sample mount.

**Angle resolved photoemission.** Measurements were made at the Spectromicroscopy beamline of the Elettra light source[1]. Linearly polarized light, at 45° to the sample, was focused to a $\sim 0.6$ μm diameter spot by a Schwarzschild objective. The photon energy was 27 eV except for the data in Fig. 1 where it was 74 eV. The hemispherical analyser with two-dimensional detector on a two-axis goniometer permitted a resolution of approximately 50 meV and 0.03 $Å^{-1}$. After mounting in the chamber on a scanning stage with 100 nm closed loop positioning accuracy, the samples were located by scanning photoemission microscopy (SPEM). With the light focus fixed, the photoelectron intensity on the detector was acquired point by point as the sample was stepped relative to the light spot. In the SPEM images the colour corresponds to the integrated photoelectron intensity around $\mathbf{\Gamma}$ (over the full detector range of ∼15°, corresponding to ∼0.6 $Å^{-1}$ at 20 eV and ∼1.1 $Å^{-1}$ at 70 eV, and binding energy range of 0 to 2.5 eV in Fig. 1d and 0 to 3.5 eV in Fig. 2c) at that point on the sample. For spectral acquisition, the entrance slit to the analyser is in a fixed orientation, but its angular coordinates relative to the sample normal are controlled by the two-axis goniometer. For energy-momentum slices along $\mathbf{\Gamma} - \mathbf{K}$, as in Figs. 2 and 3, a sequence of 2D slices was acquired with the goniometer moving the centre of the analyser entrance slit along the line in reciprocal space from $\mathbf{\Gamma} - \mathbf{K}$, mapping out a small volume in ($E,k_x,k_y$) from which the $\mathbf{\Gamma} - \mathbf{K}$ slice was later extracted. Over the few hours required to acquire this data, the sample drift was typically < 1 μm. Prior to measurement, samples were annealed in ultrahigh vacuum at 650 K for several hours. The stage temperature was ∼100 K (Figs. 2,3 and 4) or ∼105 K (Fig. 1 and $MoS_2$, $WS_2$ and $MoSe_2$). Following standard practice, we plot $E - E_F$, the negative of the electron binding energy, where $E$ is the measured photoelectron kinetic energy and $E_F$ is the kinetic energy of electrons removed from the Fermi level, determined by fitting the Fermi-Dirac distribution to the drop in photoemitted intensity across the photoemission threshold.

**Detailed considerations of gate dependence and device operation.** The devices have a thin hBN dielectric separating the graphite back-gate electrode from the upper 2D material (2DM) layer, which is either graphene itself or overlaps a graphene contact that in turn overlaps a metal (ground) electrode. When the 2DM is conducting this constitutes a parallel-plate capacitor with geometric areal capacitance $C_g = \varepsilon_0 \varepsilon_{BN}/d_{BN}$, where $\varepsilon_0$ is the relative permittivity of free space, $\varepsilon_{BN} = 4.0 \pm 0.2$ is the out-of-plane (c direction) dielectric constant for hBN, and $d_{BN}$ is the thickness of the hBN. During photoemission, the electrochemical potential at the emission spot will differ from ground, by an amount $\Delta V$, associated with current flow both to the contact and to the gate which is at voltage $V_g$,

thus reducing the effective gate voltage determining the local carrier density to $V_g - \Delta V$. $\Delta V$ will not exceed the product of the effective electrical resistance $R$ between the spot and ground electrode and the maximum current, which is no more than ~2 nA.

For **graphene devices**, the band dispersion is not affected by doping to within 10% accuracy (see Extended Data Fig. 4). In this case we expect $n_G = C_g(V_G - \Delta V - \Delta\mu/e)$, where $\Delta\mu = \Delta(E_F - E_D)$ is the chemical potential change due to gate doping (note that $C_g$ is only the geometric capacitance, and the total capacitance is nonlinear in $V_G$). For graphene, $R <$ ~1 kΩ and thus $\Delta V <$ ~2 μV, which is negligible. $\Delta\mu$ can be found from the ARPES spectrum at each gate voltage to an accuracy of ~20 meV. In the measurements shown in Fig. 1, $\Delta\mu$/e is at least ten times smaller than $V_G$, and thus simply taking $n_G \approx C_g V_G$, the quantity plotted on the top axis of Fig. 1f, is accurate to < 10%. When $k_B T \ll E_D$ (valid here since $k_B T = 9$ meV), from the conical Dirac dispersion one expects[35] $E_D^2 \approx \pi\hbar^2 v_F^2(n_0 + n_G)$, where $n_G = CV_G$ is the gate-induced 2D electron density, $C$ the areal capacitance, and $n_0$ the residual electron density at $V_G = 0$. The solid line in Fig. 1f is a fit to this model with $C$ and $n_0$ treated as fitting parameters. The value of $n_0$ obtained is $(1.8 \pm 0.1) \times 10^{12}$ cm$^{-2}$, implying a somewhat high residual doping that may be due to contamination. The value of $C$ is $(2.2 \pm 0.2) \times 10^{-7}$ Farad cm$^{-2}$, consistent with the geometrical capacitance, $\frac{\epsilon_0 \epsilon_{BN}}{d_{BN}} = (2.5 \pm 0.2) \times 10^{-7}$ Farad cm$^{-2}$, derived from the BN thickness, $d_{BN} = 14 \pm 1$ nm, measured by atomic force microscopy, and the dielectric constant, $\epsilon_{BN} = 4.0$, taken from the literature[36–38]. Note also that the intensity near $E_D$ is weak because these $E - k$ slices do not pass exactly through **K**. The much lower intensity on one side of the cone results from destructive interference between the two carbon sublattices[39].

For **$MX_2$ semiconductor devices** the situation is more complicated. At small $V_G$, the doping $n_G$ must be very small because of the band gap, so the in-plane resistance can be large and $\Delta V$ can be substantial. As long as $n_G$ is negligible the bands will not be renormalized and $\Delta V$ can be identified with the purely electrostatic energy shift of an ARPES spectral feature. $\Delta E_\Gamma/e$ in Fig. 3 indeed tracks $V_G$ closely at low $V_G$ (see Extended Data Fig. 6). We deduce that in this regime photoemission directly from the hBN valence band generates conductivity in the hBN which is sufficient to keep the potential in the $MX_2$ close to that of the gate, i.e., $\Delta V \approx V_g$, with negligible potential drop across the hBN and no accumulation of charge in the $MX_2$. In contrast, at a sufficiently large magnitude of $V_G$, $(V_G - \Delta E_\Gamma/e)$ tends towards a linear increase with $V_G$. This happens when the high doping makes in-plane resistance $R$ small enough that the electrochemical potential in the $MX_2$ approaches that in the (ground) electrode and $\Delta V$ stops changing, with the Fermi energy virtually pinned at the band edge due to the large density of states. In this regime we can take $n_G = C_g(V_G - \Delta E_\Gamma/e)$, since $V_G - \Delta E_\Gamma/e$ is the static potential drop across the hBN, the electrons are in electrochemical equilibrium, and the quantum capacitance is negligible (i.e., $E_F$ is effectively pinned at the CBE). The values of $n_G$ shown in Fig. 4 are obtained in this way.

Our interpretation of the behavior in Fig. 3 for monolayer $WSe_2$ is as follows. The photoemission current $I_{PE}$, current to the contact, $I_C$, and to the gate, $I_G$, indicated in the sketch at the top left of Fig. 3, must sum to zero. $I_G$ can be substantial because of photo-excited carriers in the BN. (It should be borne in mind that in general such currents may cause a device to operate differently from how it would in the dark). Between B and C, the $WSe_2$ is depleted and insulating enough that the BN photoconductivity brings the potential close to that of the gate. Holes created by photoemission from the $WSe_2$ recombine with excited electrons in the BN, and $I_{PE} \approx I_G$. Between C and D, these holes can also drift to the contact through the depleted $WSe_2$, and $I_C$ is significant. Above threshold, at E, electrons accumulate at the CBE in the $WSe_2$ as they flow in laterally from the graphene contact, and the CBE is pinned close to the graphene Fermi level. Similarly, at A, holes accumulate and the valence band edge is pinned. An "overshoot" occurs at D because when the CBE in the beam spot first moves below the graphene Fermi level, the Schottky barrier between graphene and $WSe_2$ prevents electrons flowing in fast enough to accumulate.

**Estimating the CBE energy**. The structure of the conduction band is not resolvable in the ARPES data (Fig. 2d-f). The density of states at a single parabolic band edge is $g_{2D} = g_s g_v m^*/\hbar^2$, with spin and valley degeneracies $g_s$ and $g_v$ and effective mass $m^*$. For 1L $WSe_2$ the conduction band edges are

at the K-points, so $g_v = 2$, and the band is spin-split by $\approx 40$ meV[40], hence $g_s = 1$ for moderate doping. Calculations[40] give $m^* \approx 0.3m_e$. Using $n_G = \int_{E_c}^{\infty} F(E) g_{2D}\, dE$, where $F(E)$ is the Fermi-Dirac distribution, then gives $E_F - E_C \approx 30$ meV at $n_G = 1.0 \times 10^{13}$ cm$^{-2}$.

**Optical spectroscopy.** Photoluminescence measurements were performed using ~20 μW linearly polarized 532 nm continuous-wave laser excitation in reflection geometry, with the signal collected by a spectrometer and a silicon charge-coupled device, in vacuum in a closed-cycle cryostat.

**Electronic structure calculations** including spin-orbit interaction were made using the Quantum Espresso DFT package[41]. Structures were first optimized until forces were smaller than $10^{-4}$ Ry / Bohr. Geometry optimisations and band structure calculations were performed with an 18×18 in-plane k-point grid with 140 Ry plane-wave energy cut off. To avoid interaction between periodic images, the vacuum spacing was 25.0 Å. We used norm-conserving fully relativistic pseudopotentials[42] from PseudoDojo[43], where the semi-core 4d, 5s and 5p states for W are retained as valence electrons. This results in a lattice constant of 3.32 Å for all three structures. We used the results from calculations with the PBE functional as a starting point for $G_0W_0$ calculations which utilised the Yambo code[44], with the Godby–Needs plasmon pole approximation[45]. We used 300 bands, 500 bands and 700 bands for the mono-layer, bilayer and trilayer $WSe_2$, respectively, for the self-energy and dynamical dielectric screening. In order to treat the divergence of the Coulomb interaction during the self-energy calculation, the random integration method[46] was used, with $3 \times 10^6$ random q-points and 100 random G vectors.

**Data availability.** All data presented in this paper are available at [*to be finalised on acceptance*]. Additional data related to this paper may be requested from the authors.


34. Zomer, P. J., Guimarães, M. H. D., Brant, J. C., Tombros, N. & Van Wees, B. J. Fast pick up technique for high quality heterostructures of bilayer graphene and hexagonal boron nitride. *Appl. Phys. Lett.* **105**, 013101 (2014).
35. Fang, T., Konar, A., Xing, H. & Jena, D. Carrier statistics and quantum capacitance of graphene sheets and ribbons. *Appl. Phys. Lett.* **91**, 092109 (2007).
36. Yu, G. L. *et al.* Interaction phenomena in graphene seen through quantum capacitance. *Proc. Natl. Acad. Sci.* **110**, 3282–3286 (2013).
37. Dean, C. R. *et al.* Boron nitride substrates for high-quality graphene electronics. *Nat. Nanotechnol.* **5**, 722–726 (2010).
38. Kim, K. K. *et al.* Synthesis and Characterization of Hexagonal Boron Nitride Film as a Dielectric Layer for Graphene Devices. *ACS Nano* **6**, 8583–8590 (2012).
39. Mucha-Kruczyński, M. *et al.* Characterization of graphene through anisotropy of constant-energy maps in angle-resolved photoemission. *Phys. Rev. B* **77**, 195403 (2008).
40. Kormányos, A. *et al.* k · p theory for two-dimensional transition metal dichalcogenide semiconductors. *2D Mater.* **2**, 022001 (2015).
41. Giannozzi, P. *et al.* QUANTUM ESPRESSO: a modular and open-source software project for quantum simulations of materials. *J. Phys. Condens. Matter* **21**, 395502 (2009).
42. Hamann, D. R. Optimized norm-conserving Vanderbilt pseudopotentials. *Phys. Rev. B - Condens. Matter Mater. Phys.* **88**, 085117 (2013).
43. van Setten, M. J. *et al.* The PSEUDODOJO: Training and grading a 85 element optimized norm-conserving pseudopotential table. *Comput. Phys. Commun.* **226**, 39–54 (2018).
44. Marini, A., Hogan, C., Grüning, M. & Varsano, D. yambo: An ab initio tool for excited state calculations. *Comput. Phys. Commun.* **180**, 1392–1403 (2009).
45. Godby, R. W. & Needs, R. J. Metal-insulator transition in Kohn-Sham theory and quasiparticle theory. *Phys. Rev. Lett.* **62**, 1169–1172 (1989).
46. Castro, A., Räsänen, E. & Rozzi, C. A. Exact Coulomb cutoff technique for supercell calculations in two dimensions. *Phys. Rev. B - Condens. Matter Mater. Phys.* **80**, 033102 (2009).